

# A Phenomenological Scattering Model for Order-Independent Transparency

Morgan McGuire  
Williams College and NVIDIA

Michael Mara  
Stanford and NVIDIA



**Figure 1:** Three scenes rendered in real-time by our method, none of which were possible under previous real-time transparency algorithms. Left) Distance-based diffusion by a frosted glass door. Center) Colored transmission with multiple layers of refraction and reflection and colored shadows with caustics. Right) Diffusion and shadowing in a participating medium with partial coverage and varying density.

## Abstract

Translucent objects such as fog, smoke, glass, ice, and liquids are pervasive in cinematic environments because they frame scenes in depth and create visually compelling shots. Unfortunately, they are hard to simulate in real-time and have thus previously been rendered poorly compared to opaque surfaces in games.

This paper introduces the first model for a real-time rasterization algorithm that can simultaneously approximate the following transparency phenomena: wavelength-varying (“colored”) transmission, translucent colored shadows, caustics, partial coverage, diffusion, and refraction. All render efficiently on modern GPUs by using order-independent draw calls and low bandwidth. We include source code for the transparency and resolve shaders.

**Keywords:** transparency, transmission, refraction, caustic, particle

**Concepts:** •Computing methodologies → Rendering;

## 1 Introduction

Occlusion is the most powerful depth cue, surpassing even perspective and shadows. Partial occlusion due to various forms of transparency gives a strong perception of depth without the limitation of concealing shape. This is one reason that film directors rely heavily on fog, smoke, and glass in cinematic composition. Another reason is that effects such as rolling fog and layered glass refraction create interesting visual complexity.

Beyond just layering, such transparent surfaces present a variety of important phenomena seen in figure 1. These include diffusion by

Permission to make digital or hard copies of all or part of this work for personal or classroom use is granted without fee provided that copies are not made or distributed for profit or commercial advantage and that copies bear this notice and the full citation on the first page. Copyrights for components of this work owned by others than the author(s) must be honored. Abstracting with credit is permitted. To copy otherwise, or republish, to post on servers or to redistribute to lists, requires prior specific permission and/or a fee. Request permissions from [permissions@acm.org](mailto:permissions@acm.org). © 2016 Copyright held by the owner/author(s). Publication rights licensed to ACM.

I3D '16, 2016-February-27

ISBN: 978-1-4503-4043-4/16/03

DOI: <http://dx.doi.org/10.1145/2856400.2856418>

frosted glass and fog, wavelength-varying transmission in colored glass, colored and translucent shadows, multiple layers of refraction, self-shadowing within dense media such as clouds, and relatively bright caustics in shadows.

Many of these phenomena have previously been hard to render efficiently under rasterization. Although there are some good special-case solutions, there is no previous real-time rasterization method that models all of them simultaneously, let alone efficiently. Thus, these important visual elements from film have been absent from real-time rendering 3D applications. This absence is particularly unfortunate because depth cues are even more important in an interactive context than in film. Game players, CAD engineers, and 3D artists need to understand depth relationships to perform tasks in 3D. Furthermore, today’s stereo screens and head-mounted virtual reality (VR) displays lack the depth cue of focal accommodation. Robust transparency by ray tracing allows ocular vergence to partly compensate for the lack of focus in pre-rendered VR content by presenting multiple viable vergences at each pixel. Our approximation brings complex transparency to real-time VR for the first time (see figure 13).

We introduce a new order-independent transparency (OIT) model for light scattering, and algorithm for rendering with it in real-time on modern GPUs. These emulate the real physical phenomena described in this section through empirically-derived methods. Our model extends previous stochastic and order-independent transparency methods that reduce complex scenes to a single amalgamated layer per pixel. This provides for efficient unordered submission of draw calls, avoids costly primitive and fragment sorting, and limits per-pixel bandwidth and storage requirements. It also has the advantage of smoothly transitioning when primitives abruptly change order, for example, eliminating the “popping” associated with particle systems under ordered transparency. Quantitatively, we demonstrate increased visual effects while achieving a 10× reduction in memory traffic compared to previous colored shadows [McGuire and Enderton 2011] alone and transparency at a 2× reduction compared to  $\alpha$ -only  $k$ -buffering [Vasilakis and Fudos 2014; Salvi and Vaidyanathan 2014].

Each approximation that we introduce contains radiometric error, compared to a ray tracer. We contend that for many real-time applications, radiometric error is less important than perceptual error. By emulating physical phenomena, our model significantly improves

the perception of transparency in many scenes compared to the alternative of no approximation of those phenomena at all.

This paper contributes new effects and demonstrates real-time performance. However, this research targets not just good performance today, but scaling with upcoming hardware architectures. After properly presenting and evaluating the method, we explain this aspect of the paper’s contribution in section 7.1.

## 2 Related Work

For each of the transparency phenomena that we model, the literature includes many real-time solutions for rendering that phenomenon *in isolation*, typically with more accuracy and higher cost than our model and with greater constraints on the scene. We review some of the most recent below. Our approach is better suited to cases where a coarser approximation is acceptable in exchange for a significant performance increase and reduction in implementation complexity, and integration of all of these phenomena into a unified transparency model.

Sorted transparency operates by the “painter’s algorithm,” rendering surfaces in back-to-front order. In addition to the sorting and ordered submission costs, it is undesirable because it requires slicing or simply fails when no consistent ordering exists between surfaces. In scenes for which a perfect ordering exists, a two-pass<sup>1</sup> implementation that first modulates the background by transmission and then adds reflected and emitted light can accurately model non-refractive transmission and partial coverage. We use that as a reference solution for those effects in our results.

***k*-buffers** Carpenter’s [1984] A-buffer was the first method for allowing order-independent submission of partial-coverage surfaces to a renderer, albeit at unbounded space and time costs for  $n$  surfaces. The  $Z^3$  method [Jouppi and Chang 1999] stores only bounded  $k$  transparent surfaces and merges the other  $n - k$  ones.  $Z^3$  hardware has never been built, but a variety of related  $k$ -buffer methods were devised for increasingly programmable, real-world GPUs [Bavoil et al. 2007; Maule et al. 2013; Salvi et al. 2011; Vasilakis and Fudos 2014; Salvi and Vaidyanathan 2014].

Parallel to the visible surface  $k$ -buffer work are methods for modeling partial coverage in the light’s view for shadowing [Lokovic and Veach 2000; Sintorn and Assarsson 2009; Jansen and Bavoil 2010] in various cumulative-opacity vs. depth curve representations.

**Stochastic Transparency** A stochastic, a.k.a. “screen door” transparency algorithm stores only one layer per sample. These methods are good for primary visibility and shadow partial coverage, but expensive because they require high (e.g.,  $128 \times$  MSA) sample counts or wide filters [Enderton et al. 2010; McGuire and Enderton 2011]. We combine this idea for shadows with the pre-filtering of Variance Shadow Maps (VSM) [Donnelly and Lauritzen 2006] to solve the performance problem.

**Blended Transparency** A key idea in the  $k$ -buffer methods is that they all aggregate the  $n - k$  overflow fragments. Meshkin [2007] proposed a blended transparency method that is essentially a  $k = 1$ -buffer, aggregating *all* fragments. He redefined the compositing operator to estimate all order-dependent terms as zero. Subsequent work [Bavoil and Myers 2008; Kluczek 2012; McGuire and Bavoil 2013] extended this through more accurate

<sup>1</sup>This can be done in one pass for monochrome transmission or on hardware with programmable blending. Fixed-function blending cannot simultaneously modulate and accumulate with  $\lambda$ -varying constants.

approximations and normalization terms. The core blending of our method advances this line of research.

**Realistic Scattering** The real-time methods we’ve described so far were all designed for simple Porter-Duff partial coverage ( $\alpha$ -blending). That’s a good model for monochrome transmission through a single-scattering medium, and is sufficient for some applications, such as rendering thin smoke and antialiasing opaque edges. However, it fails to model other real-world situations, such as color modulation of objects viewed through colored glass and the blurring seen when an object is in thick fog.

We are aware of no previous real-time diffusion solution, however there is much work on offline diffusion simulation. Nishita et al. [1998] derived early models of scattering in participating media at planetary scale. Narasimhan et al. [2003; 2004] describe how to compute a spatially-varying point spread function for diffusion in participating media based on the Legendre approximation of the Henyey-Greenstein phase function. They note that a *single* Gaussian blur is an insufficient model because it must vary at every pixel and take occlusion into account; we present exactly those extensions. Premože et al. [2004] give a derivation for the screen-space Gaussian from physical parameters.

**Refraction** The simplest refraction model is to render a dynamic environment map for each object and compute single-surface refraction of distant light. This obviously does not scale to large scenes or multiple refractions. More sophisticated recent methods include models of distant light through rough surfaces [de Rousiers et al. 2012] and screen-space layered G-buffer ray tracing [McGuire and Mara 2014; Ganestam and Doggett 2015].

**Caustics** Caustic methods have been developed for limited circumstances such as flat receivers [Yüksel and Keyser 2009], individual transmissive surfaces [Shah et al. 2007], and exactly two layers [Wyman 2005]. Wyman et al.’s [2009] recent work is extremely accurate for monochrome caustics in isolation.

## 3 Algorithm

We compute transparent phenomena in three stages. First, for each light source, we produce a colored stochastic shadow map of transmissive surfaces that is affected by caustics.

Second (after opaque surfaces have been rendered), we perform an order-independent transparency (OIT) pass. This iterates over all transparent surfaces with a pixel shader that outputs each surface’s contribution to accumulated reflected light  $A_{\text{rgba}}$ , transmission  $\beta_{\text{rgb}}$ , diffusion factor  $D$ , and refractive displacement  $\delta_{xy}$  buffers. Section 4 derives these. The appendix details configuring fixed-function blending for the required sums and products.

For surfaces such as fog particles that lack fine detail, the second stage can be performed at low resolution. We then upsample the results with a bilateral filter and combine them with full-resolution ones, allowing mixed-resolution results.

Third, we iterate over pixels in screen space that were affected by transparent surfaces to **resolve** the output of the second stage into the image of the opaque surfaces in the framebuffer.

## 4 Scattering Model

### 4.1 Material Parameters

We model transparent materials with a reflective BRDF (lambertian and microfacet + Fresnel glossy terms), emission term, partial

coverage ( $\alpha$ ), and a BTDF. Our BTDF parameters are refractive index ( $\eta$ ), wavelength-varying transmission coefficient at normal incidence ( $T(\lambda)$ ), and a collimation factor ( $c \in [0, 1]$ ). Unit collimation describes an optically homogeneous material like perfect glass that exhibits no multiple-scattering within its volume. Zero collimation describes a dense, isotropic participating medium such as muddy water or fog.

The transmission coefficient  $t(\lambda)$  used in shading is  $T(\lambda)$  modulated by one minus the BRDF, both evaluated for the actual angle of incidence. Our shading model also uses  $\bar{t}$ , the mean of  $t(\lambda)$  over wavelength.

Both the transmission coefficient and collimation factor assume that light travels a fixed distance through a medium after the surface before exiting; otherwise one would have to apply Beer’s law to accumulate their impact per pixel. This is a common real-time rendering assumption that is reasonable for drinking glasses, windows, and particles. It is a poor approximation for something like an ice sculpture that has significantly varying thickness.

Refractive index is specified once per material instead of per texel. We pack the three-channel  $T(\lambda)$  and scalar  $c$  into an sRGBA8 texture. Because  $c$  is encoded in the A channel, unspecified collimation conveniently defaults to  $c = 1$  for legacy texture maps.

## 4.2 Wavelength-Varying Blending

Consider a series of  $n$  translucent surfaces ordered from back to front towards the viewer at a pixel and an opaque backing surface that scatters radiance  $L(X_0, \lambda)$  towards the camera. (This ordering is only for the derivation. Our algorithm accepts surfaces in any order.)

The outgoing radiance towards the camera at surface point  $X_i$  and wavelength  $\lambda$  is the sum of the reflected<sup>2</sup> and transmitted light at the point [Glassner 2015]:

$$L(X_i, \lambda) = \alpha_i \cdot [L_r(X_i, \lambda) + t_i(\lambda)L(X_{i-1}, \lambda)] + (1 - \alpha_i) \cdot L(X_{i-1}, \lambda). \quad (1)$$

Here, we express the radiance that *would* exist with full coverage and then scale it for the actual coverage  $\alpha_i$  to make explicit the blending structure. The transmission coefficient  $t_i$  may vary with wavelength, and with orientation due to Fresnel effects. For the moment, we ignore refraction. No direction variable appears because we’re explicitly only measuring radiance towards the camera.

The net modulation of the background  $L(X_0, \lambda)$  after transmission through, and partial-coverage by, all translucent surfaces is exactly [McGuire and Enderton 2011]

$$\beta(\lambda) = \prod [1 - \alpha_i + \alpha_i t_i(\lambda)]. \quad (2)$$

( $\beta$  for background.) Because  $\beta$  is a product and includes *all* surfaces, order is irrelevant. Since our goal is to aggregate all surfaces into a single-layer, i.e., ( $k = 1$ )-buffer, for later composition, the net solution must be expressed in the form

$$L(X_n, \lambda) \approx \beta(\lambda) \cdot L(X_0, \lambda) + (1 - \beta(\lambda)) \cdot U(\lambda), \quad (3)$$

where  $U(\lambda)$  is a weighted sum of the radiance emitted and reflected by the translucent surfaces whose form is unknown *a priori*.

Note that the weight  $w_i$  of the contribution from layer  $i$  transmitted through, and partially covered by, surfaces  $(i+1) \dots n$  is independent of the order of those other layers [Meshkin 2007].

<sup>2</sup>we include emitted light in the “reflected” term to simplify notation

If the space between  $X_i$  and the camera were filled with a homogeneous participating medium instead of inhomogeneous discrete surfaces, then by Beer’s law, the radiance  $\alpha_i \cdot L_r(X_i, \lambda)$  scattered from surface  $i$  along the camera-space  $z$ -axis that reached the camera would be  $w_i = e^{-q|z_i|}$  [Kluczek 2012]. In that equation,  $q$  is the absorption coefficient of the medium. We can normalize by total weight to limit its influence, since we’re only computing color and the magnitude of transmission from all surfaces is known to be  $(1 - \beta)$ . This gives a solution weakly dependent on an implicit  $q$ :

$$U(\lambda) = \frac{A_{\text{rgb}}(\lambda)}{A_a} = \frac{\sum_i w_i \cdot \alpha_i \cdot L_r(X_i, \lambda)}{\sum_i w_i \cdot \alpha_i \cdot (1 - \bar{t}_i)} \quad (4)$$

We name the numerator and denominator accumulations  $A$  for later reference in the OIT stage implementation, where they are explicit RGBA buffers.

Thus far, our derivation assumed a uniform medium. Since the scene is actually filled with inhomogeneous discrete surfaces, weight  $w_i$  should not actually follow from Beer’s law but instead some scene-dependent function that is also monotonic and super-linearly decreasing in depth (because it is a product). We use

$$w_i = \min(\max([10 \cdot (1 - 0.99 \cdot f) \cdot \alpha_i \cdot (1 - \bar{t}_i)]^3, 0.01), 30) \quad (5)$$

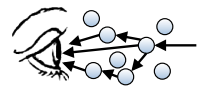
with  $f = \text{gl\_FragCoord.z}$ , which is McGuire and Bavoil’s equation 10 scaled for an infinite far plane and float16 precision.

The sums and products in  $\beta$  and  $A$  can all be computed in a single pass over transparent surfaces using multiple render targets and fixed-function blending. The appendix contains the OpenGL configuration and shaders.

## 4.3 Multiple Forward Scattering Approximation

**Diffusion** Diffusion of the background occurs when transmissive surfaces decollimate light due to repeated scattering, or due to an extremely rough transmissive interface. We explicitly model the former case and also allow artists to approximate the latter.

As depicted in the figure on the right, repeated scattering in a uniform medium produces a random walk. In screen space, this means that there is a Gaussian distribution of pixel offsets between where light enters and emerges from a surface [Premože et al. 2004]. The standard deviation of the Gaussian, and thus the diffusion in pixels, decreases with distance from the camera  $|z_i|$  (due to perspective) and with collimation  $c_i$ .



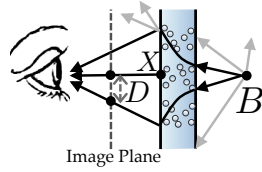
Following previous work, we estimate the total diffusion standard deviation  $D$  (in pixels) at each pixel from all foreground surfaces indexed by  $i$ , for an infinitely distant background, as

$$D = \frac{W}{2 \tan(\theta/2)} \sum_i \frac{k_0(1 - c_i)\alpha_i}{|z_i|}, \quad (6)$$

where  $\theta$  is the field of view,  $W$  is screen width in pixels, and  $k_0$  is the standard deviation (in meters) of the Gaussian due to a single  $c = 0$  surface at unit depth.

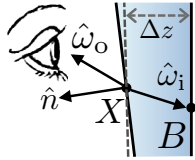
What about diffusion of background surfaces at *finite* distances? Intuitively, repeated scattering has the net effect of a collection of concave lenses; the resulting Gaussian is the sum of their point spread functions. The amount of defocus from this system increases with the distance from the surface to the background and may be close to zero. For example, a hand pressed against a frosted glass shower door will appear sharp, whereas the body behind it is diffused.

The figure on the right depicts the cone of light from background object  $B$  and its random-walk dispersion in the medium ( $B$  also scatters light that never reaches the camera, e.g., in directions shown in light gray). Let  $z_{B,i}$  be the depth of the camera-space background  $B$  as read from the depth buffer,  $z_{X,i}$  be the depth of the surface  $X$ , and constant  $k_1$  the implied thickness of the scattering surface (we simply use  $k_1 = 0.5\text{m}$  for all scenes in our results). Under this compound convex lens and the previous background model, we approximate the diffusion standard deviation for arbitrary  $B$  as:



$$D = \frac{W \cdot k_0}{2 \tan(\frac{\theta}{2})} \sqrt{\sum_i \left[ \frac{(1 - c_i) \alpha_i (1 - (1 + |z_{X,i} - z_{B,i}|/k_1)^{-1})^2}{|z_{X,i}|} \right]^2} \quad (7)$$

**Refraction of Primary Rays** Many real-time renderers approximate refraction by exactly applying Snell's law using a simplified model of the scene: a homogeneous volume of transmissive medium extending backwards to a fixed-depth background plane. Some use screen-space ray tracing to compute slightly more accurate refraction at increased cost. Both produce an offset  $(\delta_x, \delta_y)$  in pixel coordinates by which to distort the background objects already appearing in the frame-buffer.



In the absence of a principled method for combining refraction vectors from overlapping surfaces, we simply blend them. This produces a result that is as exact as previous methods for a single transmissive surface. For multiple surfaces, it is incorrect but captures the displacement phenomenon of refraction.

Consider the (camera space) ray to the center of projection from a surface point  $X$  with normal  $\hat{n}$  and relative refractive index  $\eta = \frac{\eta_{\text{before}}}{\eta_{\text{after}}}$ , in direction  $\hat{\omega}_o$ . By Snell's law, that ray refracted from direction

$$\hat{\omega}_i = -\eta \hat{\omega}_o - (\eta - \hat{n} \cdot \hat{\omega}_o + \sqrt{k}) \hat{n} \quad (8)$$

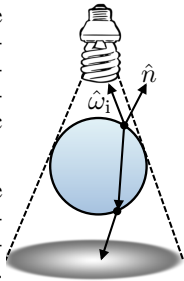
if  $k = 1 - \eta^2 [1 - (\hat{n} \cdot \hat{\omega}_o)^2]$  was non-negative (otherwise, the ray had no transmissive transport). For a background approximated as a plane at fixed depth  $\Delta z$  beyond  $X$ , the observed point is given by

$$B = X + \hat{\omega}_i \Delta z / (\hat{\omega}_i \cdot \hat{z}). \quad (9)$$

To obtain the refractive pixel offset  $(\delta_x, \delta_y)$ , we project  $B$  into screen space and subtract the current pixel coordinate.  $\Delta z$  is a per-scene parameter; we used  $\Delta z = 2\text{m}$  for all results.

**Caustics and Translucent Shadows** In the real world, focusing under refraction redistributes light within the shadowed region, producing lighter and darker areas. We approximate this by varying the density of a stochastic shadow map as follows.

Colored stochastic shadow maps [McGuire and Enderton 2011] model shadows from surfaces with wavelength-varying transmission using RGB values instead of a single depth map. During shadow map generation, they write to the shadow map for wavelength  $\lambda$  with probability  $\rho(\lambda)$  proportional to partial coverage and  $1 - \text{transmission}$ . This works because a shadow map stores surfaces of primary visibility for a light source.



To extend stochastic shadow maps to mimic caustics, we decrease shadowing where light strikes a transmissive surface at normal incidence. We increase shadowing where the refractor is at a glancing angle and thus has a low Fresnel transmission factor.

Specifically, during shadow map rendering, we increase  $\rho(\lambda)$  where the magnitude of the dot product of the surface normal  $\hat{n}$  and the vector to the light  $\hat{\omega}_i$  is close to 1, and decrease  $\rho(\lambda)$  where the dot product is close to zero. We also increase this effect with the relative refractive index  $\eta$ . Including some contrast enhancement and relevant clamping to the unit interval gives our empirically-tuned equation:

$$s = \min(\max((1/\eta - 1)/2, 0), 1) \quad (10)$$

$$g = 2 \cdot \min(\max(1 - |\hat{n} \cdot \hat{\omega}_i|^{128 \cdot s^2}, 0), 1) - 1 \quad (11)$$

$$\rho(\lambda) = (1 + g \cdot s^{0.2}) \cdot \alpha \cdot (1 - t(\lambda)) \quad (12)$$

Intuitively,  $s$  is the strength of the effect as determined by  $\eta$ , and  $g$  remaps the measure of incidence to increase its contrast.

We render one stochastic shadow map per wavelength, or a single map when the scene is known to have no wavelength-varying transmission. Stochastic shadow maps are known to require large filters to suppress noise during shading. In order to reduce the cost of this filtering, we convert the shadow maps to Variance Shadow Maps [Donnelly and Lauritzen 2006], filter them with a  $15 \times 15$  tent kernel (in two 1D passes), and downsample by a factor of four in each dimension. The resulting shadow map costs 64 bits per texel per wavelength and need only be sampled once per wavelength during shading to produce noise-free shadows.

A known limitation of VSM is light leaking under certain geometry. One could use Exponential VSM or other variants to reduce this at increased bandwidth and filtering costs. We instead accept the light leaking for translucent shadows (since the shadow is already translucent, the additional light is often acceptable) and use a separate traditional Williams shadow map for opaque shadows.

## 5 Resolve Stage

The resolve stage comprises optional upsampling followed by a full-screen pass implemented as pixel shading of a screen-space quad, or as a compute shader. It performs the following steps:

**Upsample** When accumulating particles at low resolution, we begin the resolve pass by joint-bilateral upsampling the low-resolution buffers as if they were simply colors, using the depth buffer as a key. See Tatarchuk [2013] for filtering details. We use a  $7 \times 7$  tent filter kernel and composite the result of the upsample into the full-resolution buffers using the same blending modes as for the transparency stage (see the appendix), except that the render target with index 1 (RT1) uses `glBlendFuncSeparate(1, GL_ZERO, GL_SRC_COLOR, GL_ONE, GL_ONE)`.

**Refract** For each pixel  $(x_0, y_0)$  in the output, we read from the transparent buffers at  $(x_0, y_0)$  but sample the background with a filter centered around  $(x, y) = (x_0, y_0) + \delta_{xy}$ . Note that transparent surfaces cannot refract one another under this model.

**Diffuse** We gather from the background according to a Gaussian point spread function [Premoze et al. 2004] with standard deviation  $D$  (this is a single pixel when  $D = 0$ ) for diffusion. Some coefficients in the kernel must also be zeroed out to model occlusion by nearer opaque objects. We do this by gathering at output pixel  $(x, y)$  only from pixels  $(x + i, y + j)$  at which

$\min(D[x, y], D[x + i, y + j]) \leq \|(i, j)\|$ . This filter is unfortunately not separable and is thus expensive when  $D$  is large. Recognizing that this is similar to depth-of-field (DoF) rendering with the circle-of-confusion parameter replaced by  $D$ , we speculate that techniques from DoF methods could accelerate diffusion.

**Modulate and Combine** Transmissive modulation of the opaque background as captured in  $\beta$  is exact. However, transmissive surfaces don't modulate each other in the  $A$  channels, so sometimes they have an ambiguous appearance where they overlap in the image. For example, a white glossy highlight on a distant glass surface will not be colored in  $A$  by a foreground glass object with highly saturated transmission color through which it is observed (see figure 8). To compensate for this, we blend 50% of the hue of  $\beta$  into  $A$  when we normalize by the sum of the weights in  $A_a$ :

$$U' = \frac{A_{\text{rgb}}}{A_a} \left[ \frac{1}{2} + \frac{\beta}{2 \max(\max(\beta), \epsilon)} \right] \quad (13)$$

We call the term in brackets *self-modulation* because it applies a portion of the  $\beta$  modulation to the transmissive surfaces themselves.

With the background value filtered by diffusion and refraction and  $A$  and  $\beta$  sampled from the buffers, we compute  $U'$  and then simply apply equation 3 to compute the final pixel radiance.

## 6 Results

### 6.1 Evaluation of Isolated Phenomena

Figure 2 shows a grid of two layers of colored transmissive glass bars rendered with three algorithms. Like real glass, these glossy reflect “white”, have no diffuse reflection, and transmit the color that they appear. Previous recent OIT methods fail to model transmission, so they can only approximate colored glass with monochrome partial coverage (left). For this hard test case, our results (center) exactly match two-pass sorted transparency (right).

Figure 3 shows a scene with a row of teapots behind panes of glass. The panes have decreasing collimation from left to right. The top row was rendered with offline path tracing in previous work by others<sup>3</sup>. We attempted to recreate their scene from that image, and then rendered our real-time result on the bottom, which captures similar phenomena. Note also the decreased diffusion of the checkered box compared to the teapots in both rows, which occurs because the box is pressed against the glass.

Figure 4 compares shadows from three algorithms. The rightmost two objects are our stochastic VSM shadows with caustics. They match the expected phenomena for the cloud (translucency proportional to distance traveled) and the refractive sphere (caustic in the center). The correct darkening of the lower portion of the cloud itself is due to self-shadowing within that medium; the shading normals are identical on all particles.

Figure 5 shows how the caustic approximation varies as expected with  $\eta$ . We use a sphere for clarity and then gives a example of more complex geometry. Figure 6 shows a detail of the caustic stochastic shadow map for this scene before conversion to VSM, where its screen-door nature is apparent. The ground plane is a gradient instead of constant because spotlight is inclined. For another example, refer to the caustics from the glass tumblers and ice cubes in figure 1(center).

Figure 8 shows overlapping colored transmission of plastic (i.e., nonrefracting) bottles under four methods. The yellow arrows point

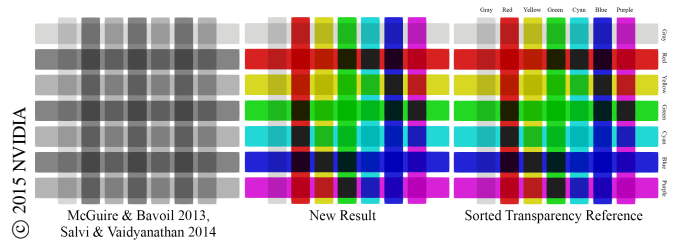


Figure 2: Colored transmission through two layers of glass bars.

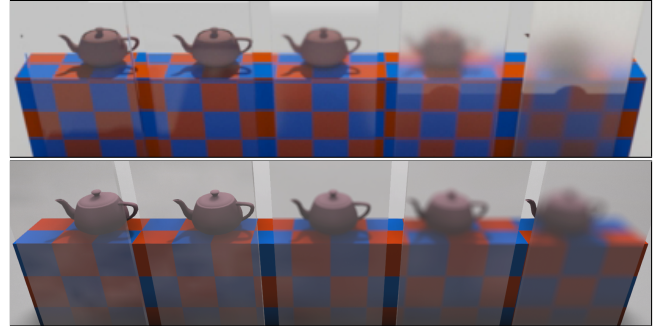


Figure 3: Top: Decreasing collimation, rendered by offline path tracing in iRay. Bottom: Our real-time result. © 2015 NVIDIA

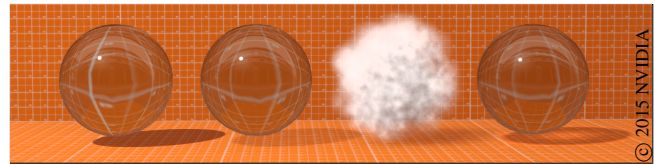


Figure 4: Left to right: Williams' opaque shadow map, Enderton et al.'s stochastic shadow map, and our phenomenological caustic stochastic shadow map applied to a cloud (no refraction, no caustic) and glass sphere (producing a refractive caustic).

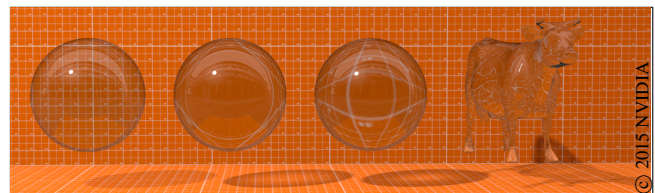


Figure 5: Caustic stochastic shadow map shadows for varying refractive indices. From left to right:  $\eta = 1.0$  (air), 1.3 (ice), 1.5 (glass), 1.5.

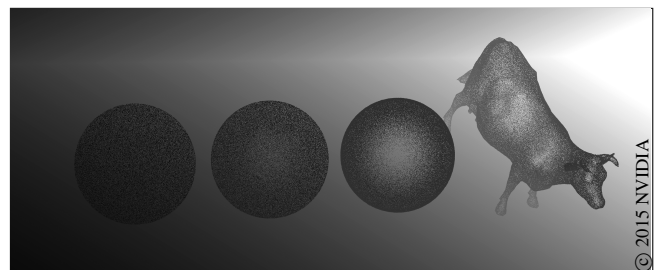
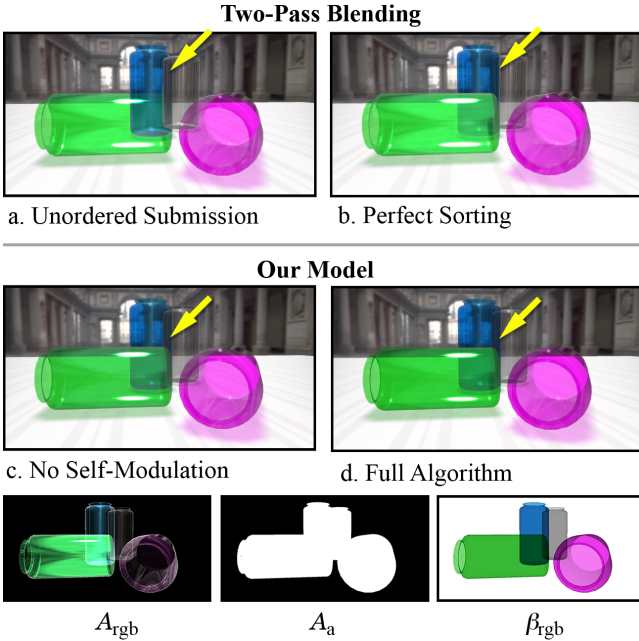


Figure 6: Visualization of a caustic stochastic shadow map.

<sup>3</sup>From the iRay developer blog at <http://blog.irayrender.com/post/19731699592/frosted-glass-part-ii>



**Figure 7:** A glass chess set rendered with two draw calls and naive blending vs. our method in a single draw call for all transmissive surfaces. The  $\delta_{xy}$  term is visualized as RGB color  $((\delta_x + 1)/2, (\delta_y + 1)/2, 0)$ . Arrows point to some errors in the naive rendering. Our result corrects the ordering and captures the phenomena of colored shadows with caustics, refraction, and colored transmission. © 2015 NVIDIA



**Figure 8:** Four plastic bottles on a table in the Uffizi rendered by different methods (all using our shadowing). The overlaid yellow arrows denote a challenging area. a) Two-pass blending with unordered submission is obviously incorrect. b) Perfect sorting gives an ideal but result in  $2n$  draw calls. c) Our method without self-modulation is efficient but has weak coloring in some areas. d) Self-modulation improves overlaps. © 2015 NVIDIA

to one challenging area. Subfigure (a) shows what two-pass sorted blending produces with *unordered* primitive submission; the performance is good and quality is unacceptable. Subfigure (b) shows that  $2n$  draw calls for  $n$  objects with perfect sorting yield ideal quality, albeit at low performance. Subfigure (c) shows our algorithm with the self-modulation term disabled; some areas of colored overlap give an ambiguous appearance. Subfigure (d) shows our final result, in which  $\beta$  modulates  $A$  during the resolve pass using equation 13. This result is qualitatively close to optimal (b) in terms of disambiguating overlaps, but slightly increases color saturation because surfaces must also modulate their own reflections. The bottom row shows the intermediate buffers.

## 6.2 Complex Scenes with Simultaneous Phenomena

The left and right subimages of figure 1 show diffusion in complex noir scenes. Figures 10a and 10b visualize the diffusion channel  $D$  for these. Both scenes exhibit diffusion increasing with depth, but for different reasons. In the first scene, objects become more diffused as the distance  $|z_{X,i} - z_{B,i}|$  from the single frosted glass sur-

face increases. The door frame and text have  $D = 0$  because they are in front of the glass. The man, woman, and far wall are progressively distant behind the glass and therefore increasingly diffused.

In the second scene, objects become more diffused as the thickness of the medium increases because there are more surfaces  $i$  in the summation. The woman is not very diffused because very little fog is between her and the camera. The man deep in fog is more diffused and the buildings are blurred beyond recognition. As the lamp posts recede into the fog, they become more diffused.

Figure 7 shows a red and clear glass chess set in a living room. On the left is two-pass blending applied to objects. Because all chess pieces with the same material are a single mesh, there is no correct sorting order. Furthermore, shadows don't capture transparency and there is no refraction. Our result in the center fixes these problems and is rendered in a single draw call for all transparent surfaces. A visualization of the intermediate buffers is on the right.

Figure 9 shows a CAD model of an automobile engine rendered in two orientations by our method. The orientation is clear in each case due to weighted blending. This is a challenging case because the surfaces are in close proximity and all have partial coverage.

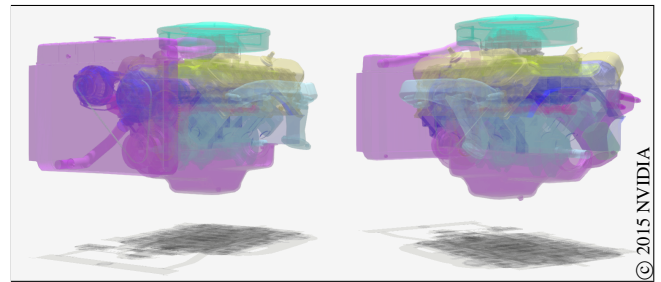


**Figure 9:** CAD-style rendering of a car engine with many closely-packed partial-coverage surfaces, in two orientations.

Figure 11 compares hair under three methods. We include this for completeness, but do not claim it is a strongly-motivating case for our method. A head of hair has a very narrow depth range, so all weights  $w_i$  are nearly uniform across it. Our model doesn't produce a result substantially better than unsorted blending. Because hair is a special case in which a uniform partial-coverage material quickly saturates to full opacity and in many cases covers a minority of the screen, we propose using a  $k$ -buffer or other bandwidth-intensive method (see Yuksel and Tariq's survey [2010]) to render hair to a small off-screen texture and then compositing that as a single aggregate surface under our model. This would improve quality while still integrating with a general method.

Figure 12 shows two versions of a scene with overlapping transmissive glass and partial-coverage smoke. The left image uses a  $4 \times 4$  subsampling for the smoke buffers. Because the transparent



(a) One layer of glass (b) Dense fog

Figure 10: Diffusion channel  $D$  for scenes from figure 1.



Unsorted Blending Sorted Blending Our Model

Figure 11: Heads with 50k  $\alpha = 0.2$  hairs totaling 24M polygons each, rendered under three transparency strategies with stochastic shadow maps for self-shadowing. © 2015 NVIDIA

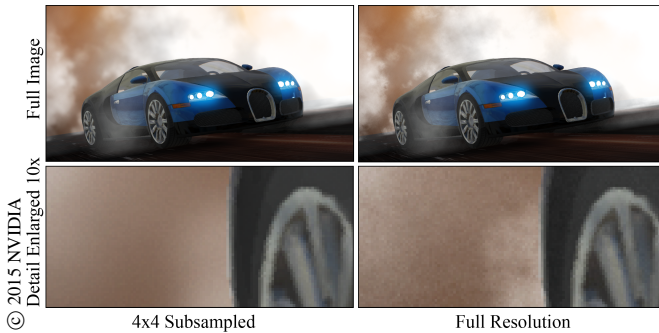


Figure 12: Overlapping glass and smoke at varying resolutions.

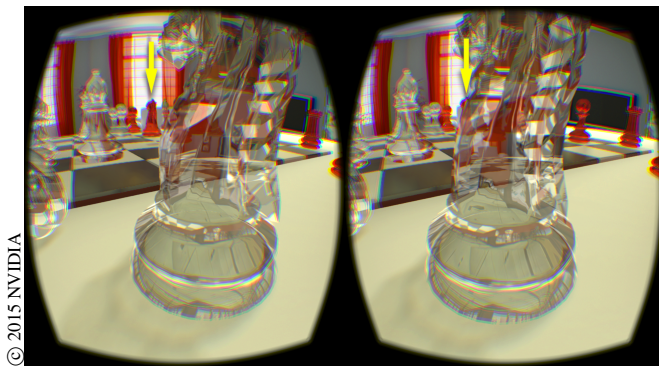


Figure 13: Chess scene rendered to the Oculus DK2 HMD.

pass rendering time is dominated by the smoke, this gives nearly a  $16\times$  bandwidth reduction and proportional speedup. Glass is at full resolution in both images. While some fine detail is of course lost due to subsampling, note that opaque and transparent objects meet at clean edges due to the bilateral upsampling and that in the final images, areas where the glass and smoke overlap are nearly identical even though smoke was processed separately on the left.

We also implemented our algorithm for the Oculus VR SDK. Figure 13 shows the head-mounted display (HMD) image with precor-

Table 1: Run time in milliseconds for each stage of our algorithm.

Scene	Figure	1. Shadow	2. OIT	3. Resolve
Door	1 left	0.01 + 1.55	0.04	2.37
Glasses	1 center	0.73 + 4.65	1.53	0.09
Foggy Night	1 right	0.37 + 1.55	4.32	4.02
w/ $4\times 4$ sub.	-	0.37 + 1.55	0.37	5.01
Chess	7	0.24 + 4.65	6.21	0.09
Engine	9	0.48 + 1.55	10.0	0.07
Hair (24 Mtris)	11	28.13 + 1.55	19.21	0.06
Car	12 right	0.68 + 1.55	2.91	0.11
w/ $4\times 4$ sub.	12 left	0.68 + 1.55	0.25	1.10
San Miguel	14	5.07 + 1.55	0.54	0.09

rection for its optical distortion. The overlaid yellow arrows mark a red chess knight in the background seen directly by the left eye and observed through the foreground clear piece by the right. Evaluating recent transparency methods for HMDs is future work, however we report that the ability to “focus” one’s vergence on either the foreground or the background knight felt surprisingly like true focal accommodation to us. Here and in the noir scenes, we had a much stronger sense of depth and presence than when we removed the fog or turned the glass objects opaque—those changes made the HMD’s fixed focal plane more apparent and made depths more ambiguous.

Figure 14 shows the San Miguel scene, which has significant partial coverage at foliage silhouettes as well as glass transmission on windows, lamps, and wine glasses. Note that only the silhouettes of leaves and not the interiors appear in the OIT buffers—those surfaces render in the opaque rendering pass where  $\alpha = 1$ .

Table 1 gives the run time for each stage of our algorithm on an NVIDIA GeForce 980 GPU at  $1920\times 1080$  resolution. We render shadow maps at  $4096^2$  resolution and filter them down to  $1024^2$  VSMs. The first number in the Shadow column is the geometry-dependent depth map generation time. The second number is VSM creation time, which depends only on the number of lights and wavelengths.

The Order-Independent Transparency (OIT) stage 2 is dominated by the cost of shading the surfaces themselves—the weighting and refraction calculations in listing 1 add only about 25 arithmetic operations and one texture fetch. Recall that the Hair scene has 24M sub-pixel triangles and thus a high render time.

The Resolve stage 3 is extremely fast when there is no upsampling or diffusion. Subsampling smoke and fog produces better than an order of magnitude throughput increase at the OIT stage, with the cost of a fixed  $\approx 1$  ms overhead for upsampling in the Resolve stage. Diffusion running time is linear in the number of non-zero elements of the point-spread kernels ( $\propto D^2$ ).

## 7 Discussion

### 7.1 Impact in the Context of GPU Architecture

We described a method that extends the previous weighted-blended transparency methods with several new effects and demonstrated their visual impact and performance. Moreover, this research targets not just high performance today, but scaling with longer-term trends in hardware architecture.

Our method requires only fixed-function blending during frame-buffer writes. Thus, it avoids the pixel-synchronization overhead of programmable blending on new GPUs. This is important because synchronization points *limit* parallelism, and scaling to upcoming 4k TVs and head-mounted displays will require *more* parallelism than even today’s best GPUs. In the short term, avoiding



**Figure 14:** Several views in *San Miguel* and intermediate buffers. Note overlapping partial coverage (leaves) and transmissive and refractive (glass) surfaces. © 2015 NVIDIA

synchronization also allows implementation on widely deployed DX11/GL4-class GPUs, including consoles.

Memory bandwidth is a limiting constraint on high-performance rendering [Whitted 2010]. That is because off-chip DRAM and its physical interface have changed relatively little over the past 50 years. Hence, bandwidth increased slowly compared to the Moore’s Law pace of arithmetic operations. In fact, the open secret of early GPUs was that their advantages over CPUs were large texture caches and wide memory interfaces, and not flops/s.

NVIDIA’s upcoming 2016 Pascal GPU architecture stacks DRAM on top of the processor for a one-time higher-bandwidth interface [Huang 2015]. However, because every surface on the package is now occupied, we will never see another comparable increase under DRAM with metal interconnects. Thus, while we predict a brief upset for a few months, in the long term, increased performance will be achieved only by decreasing memory traffic to take advantage of the steady arithmetic scaling offered by massive parallelism.

Our full algorithm requires only 112 bits/pixel of framebuffer write bandwidth and storage during the key Transparency stage 2. For  $\alpha$ -only scenes, this drops to 88 bits/pixel. In comparison, Salvi and Viadyanathan’s method [2014] with a ( $k = 4$ )-buffer for  $\alpha$  requires 256 bits/pixel and Vasilakis and Fudos’s method [2014] requires between 128 and 320 bits/pixel in the worst case. Thus, our approach has strictly higher throughput for this stage by up to  $3.6\times$  for  $\alpha$ -only, and our full model achieves a  $2\text{-}3\times$  increase vs. previous  $\alpha$ -only methods.

For casting transparent shadows on all scene elements, McGuire and Enderton’s [2011] method requires around 176 texture fetches for the  $15\times 15$  tent filter that eliminates stochastic noise. By combining their method with VSM [Donnelly and Lauritzen 2006], we reduced that to a single fetch per shaded fragment. Combined with the geometry-independent prefiltering process, this is about a  $15\times$  net bandwidth reduction for the scenes in our experiments.

## 7.2 Limitations and Future Work

Despite their run-time costs and limitations, we find the quality of special-purpose hair and caustic methods compelling and desire that quality combined with our method’s performance.

“Subsurface scattering” is the result of diffusion in a dense, highly-scattering transparent medium. We’d like to reconcile transparency and real-time subsurface scattering (e.g., [Jimenez et al. 2010]) models, and ideally unify their algorithms.

Ours and all other order-independent transparency methods inherently interact poorly with screen-space effects such as reprojection antialiasing, ambient occlusion, screen-space reflection, motion blur, and depth of field because there is no single depth corresponding to each pixel in the final framebuffer.

One obvious future direction is to replace both translucency and screen-space effects with ray tracing. Today, a rasterization renderer with our method and various screen-space effects is about an order of magnitude faster than a comparable ray tracing one. For games, rasterization-and-approximation performance trumps the challenges that this poses for software engineering and artists to work within the approximations. However, at some point the opposite tradeoff may be worthwhile, using more machine time to reduce the cost of authoring software and content. The natural questions for further research are what new algorithms and architectures would enable this inflection point, and since there is unlikely to be an instantaneous change, how they can smooth the transition from an all-rasterization to an all-ray tracing pipeline.

## References

- BAVOIL, L., AND MYERS, K. 2008. Order independent transparency with dual depth peeling. Tech. rep., NVIDIA.
- BAVOIL, L., CALLAHAN, S. P., LEFOHN, A., COMBA, J. L. D., AND SILVA, C. T. 2007. Multi-fragment effects on the GPU using the  $k$ -buffer. In *Proc. of I3D*, ACM, 97–104.
- CARPENTER, L. 1984. The A-buffer, an antialiased hidden surface method. In *Proc. of SIGGRAPH*, ACM, 103–108.

DE ROUSIERS, C., BOUSSEAU, A., SUBR, K., HOLZSCHUCH, N., AND RAMAMOORTHY, R. 2012. Real-time rendering of rough refraction. *IEEE Trans. on Vis. and Comp. Graph.* (Feb).

DONNELLY, W., AND LAURITZEN, A. 2006. Variance shadow maps. In *Proc. of I3D*, ACM, 161–165.

ENDERTON, E., SINTORN, E., SHIRLEY, P., AND LUEBKE, D. 2010. Stochastic transparency. In *Proc. of I3D*, ACM, 157–164.

GANESTAM, P., AND DOGGETT, M. 2015. Real-time multiply recursive reflections and refractions using hybrid rendering. *Vis. Comput.* 31, 10 (Oct.), 1395–1403.

GLASSNER, A. 2015. Interpreting alpha. *JCGT* 4, 2 (May), 30–44.

HUANG, J.-H., 2015. Keynote, March. GPU Technology Conference, San Jose, CA.

JANSEN, J., AND BAVOIL, L. 2010. Fourier opacity mapping. In *Proc. of I3D*, ACM, 165–172.

JIMENEZ, J., WHELAN, D., SUNDSTEDT, V., AND GUTIERREZ, D. 2010. Real-time realistic skin translucency. *CG&A* 30, 4, 32–41.

JOUPPI, N. P., AND CHANG, C.-F. 1999.  $Z^3$ : an economical hardware technique for high-quality antialiasing and transparency. In *Proc. of Graphics Hardware*, ACM, 85–93.

KLUCZEK, K., 2012. Efficient rendering of intersecting soft particles, September. Talk at WGK, Poland.

LOKOVIC, T., AND VEACH, E. 2000. Deep shadow maps. In *Proc. of SIGGRAPH*, ACM, 385–392.

MAULE, M., COMBA, J., TORCHELSEN, R., AND BASTOS, R. 2013. Hybrid transparency. In *Proc. of I3D*, ACM, 103–118.

MCGUIRE, M., AND BAVOIL, L. 2013. Weighted blended order-independent transparency. *JCGT* 2, 2 (December), 122–141.

MCGUIRE, M., AND ENDERTON, E. 2011. Colored stochastic shadow maps. In *Proc. of I3D*, ACM, 89–96.

MCGUIRE, M., AND MARA, M. 2014. Efficient GPU screen-space ray tracing. *JCGT* 3, 4 (December), 73–85.

MESHKIN, H., 2007. Sort-independent alpha blending, March. Perpetual Entertainment, GDC Session.

NARASIMHAN, S. G., AND NAYAR, S. K. 2003. Shedding light on the weather. In *Proc. of CVPR*, IEEE, 665–672.

NARASIMHAN, S. G., RAMAMOORTHY, R., AND NAYAR, S. K. 2004. Analytic rendering of multiple scattering in participating media. Tech. rep., Columbia University.

NISHITA, T. 1998. Light scattering models for the realistic rendering of natural scenes. In *Proc. of E.G.*, Eurographics, 1–10.

PREMOŽE, S., ASHIKHMIN, M., TESSENDORF, J., RAMAMOORTHY, R., AND NAYAR, S. 2004. Practical rendering of multiple scattering effects in participating media. In *Proc. of EGSR*, Eurographics, 363–374.

SALVI, M., AND VAIDYANATHAN, K. 2014. Multi-layer alpha blending. In *Proc. of I3D*, ACM, 151–158.

SALVI, M., MONTGOMERY, J., AND LEFOHN, A. 2011. Adaptive transparency. In *Proc. of HPG*, ACM, 119–126.

SHAH, M. A., KONTINEN, J., AND PATTANAIK, S. N. 2007. Caustics mapping: An image-space technique for real-time caustics. *IEEE Trans. Vis. Comput. Graph.* 13, 2, 272–280.

SINTORN, E., AND ASSARSSON, U. 2009. Hair self shadowing and transparency depth ordering using occupancy maps. In *Proc. of I3D*, ACM, 67–74.

TATARCHUK, N., TCHOU, C., AND VENZON, J., 2013. Mythic science fiction in real-time: Destiny rendering engine, July. SIGGRAPH Advances in Real-Time Rendering in Games Course.

VASILAKIS, A. A., AND FUDOS, I. 2014. K+-buffer: Fragment synchronized k-buffer. In *Proc. of I3D*, ACM, 143–150.

WHITTED, T., 2010. Disaggregated graphics: Rich clients for clouds, June. Keynote at HPG.

WYMAN, C., AND NICHOLS, G. 2009. Adaptive caustic maps using deferred shading. *Computer Graphics Forum*.

WYMAN, C. 2005. An approximate image-space approach for interactive refraction. *ACM Trans. Graph.* 24, 3, 1050–1053.

YUKSEL, C., AND KEYSER, J. 2009. Fast real-time caustics from height fields. *Vis. Comput.* 25, 5-7 (Apr.), 559–564.

YUKSEL, C., AND TARIQ, S. 2010. Advanced techniques in real-time hair rendering and simulation. In *SIGGRAPH Courses*, ACM, 1–168.

## Appendix: Implementation Details

**Render Targets** Configure four OpenGL framebuffer render target (RT) attachments as specified in table ?? for the OIT stage. All targets use the additive blend equation `glBlendEq(GL_ADD)`. For the blending function, RT1 uses `glBlendFuncSeparate(1, GL_ZERO, GL_ONE_MINUS_SRC_COLOR, GL_ONE, GL_ONE)` and RT0 and RT2 use `glBlendFunc(GL_ONE, GL_ONE)`.

On platforms without separate alpha blending, move  $D$  to the third channel of RT2. Doing so intuitively packs all multiple scattering terms into RT2, but costs another 16 bits because a modern GPU will align each 24-bit texture to 32 bits per pixel. For platforms without SNORM formats, scale and bias RT2.

Particle systems often contain many surfaces that each have low coverage ( $\alpha$ ), which raises the issue of underflow in the Transparency stage. We round non-zero values less than  $1/255$  up to  $1/255$  in the  $D$  channel, which creates slight over-diffusion but avoids underflow. We find that underflow in  $\beta$  is often imperceptible.

**Table 2:** Framebuffer layout.  $(1/63)$  factors give roughly  $\frac{1}{2}$ -pixel precision on refraction and diffusion.

	Encoding	Format	Bits/Pix	Clear Value
RT0	$(A_r, A_g, A_b, A_a)$	RGBA16F	64	(0, 0, 0, 0)
RT1	$(\beta_r, \beta_g, \beta_b, D^2/63^2)$	RGBA8	32	(1, 1, 1, 0)
RT2	$(\delta_x, \delta_y)/63$	RG8SNORM	16	(0, 0)

**Pixel Shader** In our experiments, we used the standard G3D Innovation Engine (<http://g3d.cs.williams.edu>) surface pixel shaders for the Transparent stage, with the output changed to write to the  $A, \beta, D, \delta$  buffers instead of a single color framebuffer using the code from listing 1. Position  $x$  and normal  $n$  are in camera space. Variable names match section 4. Listing 2 is the GLSL implementation of the resolve stage.

```

void computeOutput(vec3 L_r, float alpha, vec3 t,
float c, float eta, vec3 X, vec3 n, out vec4 A,
out vec3 beta, out float D, out vec2 delta) {

float netCoverage =
alpha * (1.0 - dot(t, vec3(1.0/3.0)));
float tmp = (1.0 - gl_FragCoord.z * 0.99) *
netCoverage * 10.0;
float w = clamp(tmp * tmp * tmp, 0.01, 30.0);

float z_B = depthToZ(texelFetch(depthBuffer,
ivec2(gl_FragCoord.xy), 0).r, clipInfo);

vec2 refractPix = refractOffset(n, X, eta);
const float k_0 = 120.0 / 63.0, k_1 = 0.05;

A = vec4(L_r * alpha, netCoverage) * w;
beta = alpha * (vec3(1.0) - t) * (1.0 / 3.0);
D = k_0 * netCoverage * (1.0 - c) *
(1.0 - k_1 / (k_1 + X.z - z_B)) / abs(X.z);
delta = refractPix * netCoverage * (1.0 / 63.0);

D *= D; // Store D2, variance, during summation
if (D > 0.0) D = max(D, 1.0 / 256.0);
}

```

**Listing 1:** Pixel shader outputs for Transparency stage 2.

```

#version 330 compatibility
// Typical GLSL preprocessor and math helpers from
// http://g3d.cs.williams.edu
#include <compatibility.glsl>
#include <g3dmath.glsl>

uniform sampler2D ATex, BDTex, deltaTex;
uniform sampler2D bkgTexture;

out Color3 result;

// Pixels per unit diffusion std dev
const float PPD = 200.0;
const int maxDiffusionPixels = 16;

#define fetch(a, b) texelFetch(a, b, 0)

void main() {
vec2 bkgSize = textureSize(bkgTexture, 0).xy;
int2 C = int2(gl_FragCoord.xy);
vec4 BD = texelFetch(BDTex, C, 0);
vec3 B = BD.rgb;
if (minComponent(B) == 1.0) {
// No transparency
result = fetch(bkgTexture, C).rgb;
return;
}

float D2 = BD.a * square(PPD);
vec2 delta = fetch(deltaTex, C).xy * 0.375;

vec4 A = fetch(ATex, C);
// Suppress under- and over-flow
if (isinf(A.a)) A.a = maxComponent(A.rgb);
if (isinf(maxComponent(A.rgb)))
A = vec4(isinf(A.a) ? 1.0 : A.a);

// Self-modulation
A.rgb *= vec3(0.5) +
0.5 * B / max(0.01, maxComponent(B));
}

```

```

// Refraction
vec3 bkg = vec3(0);

if (D2 > 0) { // Diffusion

C += int2(delta * bkgSize);
// Tap spacing
const float stride = 2;
// Kernel radius
int R = int(min(sqrt(D2), maxDiffusionPixels) /
float(stride)) * stride;

float weightSum = 0;
for (vec2 q = vec2(-R); q.x<=R; q.x+=stride) {
for (q.y = -R; q.y<=R; q.y+=stride) {
float radius2 = dot(q, q);

if (radius2 <= D2) {
int2 tap = C + ivec2(q);
float t = fetch(BDTex, tap).a;
float bkgRadius2 = t * PPD*PPD;

if (radius2 <= bkgRadius2) {
// Disk filter (faster, looks similar)
float w = 1.0 / bkgRadius2 + 1e-5;

// True Gaussian filter
//float w=exp(-radius2/(8*bkgRadius2)) /
//sqrt(4*PI * t);

bkg += w * fetch(bkgTexture, tap).rgb;
weightSum += w;
}}}}
bkg /= weightSum;
} else {
// No diffusion (+ fractional refraction)
bkg = textureLod(bkgTexture,
delta + gl_FragCoord.xy / bkgSize, 0).rgb;
}

result = bkg * B + (vec3(1) - B) * A.rgb /
max(A.a, 0.00001);
}

```

**Listing 2:** Pixel shader for Resolve stage 3 with common, constant-time implementation optimizations.

## Acknowledgements

We thank David Luebke, Dan Evangelakos, and our colleagues in the architecture group at NVIDIA for their assistance; anonymous reviewers for their suggestions; the ACM for requiring copyright statements on each image; Cem Yuksel for the hair model; and Guillermo Llaguno for San Miguel. Other scene elements were purchased from TurboSquid.